Supporting Information Available

NIR Afterglow Luminescent AIE dots with Ultrahigh Tumor-to-Liver Signal Ratio for Promoted Image-Guided Cancer Surgery

Xiang Ni,[†,#] Xiaoyan Zhang,[†,#] Xingchen Duan,[†] Han-Liang Zheng,[‡] Xiao-Song Xue,[‡] and Dan Ding[*,†]*

[†]State Key Laboratory of Medicinal Chemical Biology, Key Laboratory of Bioactive Materials, Ministry of Education, and College of Life Sciences, and [‡]State Key Laboratory of Elemento-Organic Chemistry, and College of Chemistry, Nankai University, Tianjin 300071, China

Corresponding Author

*Tel/fax: +86-22-2350-1229; e-mail: dingd@nankai.edu.cn

Experimental Section

Chemicals. All the chemicals were obtained from Sigma-Aldrich unless otherwise specified, and used as received without further purification. 1,2-Distearoyl-*sn*-glycero-3-phosphoethanolamine-*N*-[methoxy(polyethylene glycol)-2000] (DSPE-PEG_{2000}; Lipid-PEG_{2000}) was purchased from Laysan Bio, Inc. (Arab, AL). The solvents for chemical reactions were distilled before use. Milli-Q water was supplied by Milli-Q Plus System (Millipore Corporation, Breford, USA). Compounds **1**, **3**, **4**, **9**, **10**, and Ph-DCM were synthesized according to the literature.[1,2]

Characterization. ^{1}H and ^{13}C NMR spectra were recorded on a Bruker-DPX 400 spectrometer. Chemical shifts are reported in ppm from tetramethylsilane with the solvent resonance as the internal standard. High-resolution mass spectra (HRMS) were recorded on a Varian 7.0T FTMS Mass Spectrometer System operating in Matrix-Assisted Laser Desorption/Ionization Time of Flight (MALDI-TOF) mode. UV-vis absorption spectra were recorded on a Shimadzu UV-1700 spectrometer. Photoluminescence and afterglow spectra were recorded on a Perkin-Elmer LS 55 spectrofluorometer. The observation of nanoparticle morphology was investigated using transmission electron microscopy (TEM, JEM-2010FJEOL, Japan). Size distribution of nanoparticles was conducted on dynamic light scattering (DLS) with a particle size analyzer (90 Plus, Brookhaven Instruments Co. USA) at a fixed angle of 90^{o} at room temperature. Afterglow images and NIR fluorescent images were acquired using the Xenogen IVIS® Lumina II system under bioluminescence and fluorescence modes, respectively.

Synthesis of TPE-DCM and TPE-Ph-DCM. The intermediates **7** and **8** were firstly synthesized from compound **5** according to the literature.[3,4] To a stirred solution of TPE-

aldehyde (compounds **7** and **8**, respectively; 1.0 equiv) and compound **9** (1.0 equiv) in dry acetonitrile, piperidine (0.1 equiv) was added under argon atmosphere. The solution was heated to reflux for 12 h. The reaction mixture was filtered. The residue was washed with acetonitrile and dried in vacuum to give TPE-DCM and TPE-Ph-DCM, respectively.

TPE-DCM (80 mg, 27.6 % yield) was obtained from compound **7** (200 mg, 0.476 mmol) as a red solid. ^{1}H NMR (400 MHz, $CDCl_3$) δ (ppm): 8.90 (d, J = 8 Hz, 1H), 7.72 (t, J = 8 Hz, 1H), 7.55-7.52 (m, 2H), 7.44 (t, J = 8 Hz, 1H), 7.32 (d, J = 8 Hz, 2H), 7.14-7.12 (m, 3H), 7.09-7.03 (m, 4H), 6.98-6.93 (m, 4H), 6.81 (s, 1H), 6.71 (d, J = 16 Hz, 1H), 6.68-6.63 (m, 4H), 3.75 (d, J = 4 Hz, 6H). ^{13}C NMR (101 MHz, $CDCl_3$) δ (ppm): 158.48, 158.33, 157.64, 152.79, 152.34, 147.31, 143.78, 141.65, 138.84, 138.30, 135.99, 135.92, 134.59, 132.68, 132.62, 132.21, 132.19, 131.43, 127.91, 127.46, 126.43, 125.93, 125.82, 118.58, 117.95, 117.86, 116.84, 115.73, 113.23, 113.06, 106.66, 62.54, 55.13, 55.11. HRMS (MALDI-TOF): *m/z* calcd. for $C_{42}H_{30}N_2O_3$: 610.2256; found: 610.2255.

TPE-Ph-DCM (110 mg, 39.8 % yield) was obtained from compound **8** (200 mg, 0.403 mmol) as a red solid. ^{1}H NMR (400 MHz, $CDCl_3$) δ (ppm): 8.93 (d, J = 8 Hz, 1H), 7.75 (t, J = 8 Hz, 1H), 7.68-7.61 (m, 5H), 7.57 (d, J = 8 Hz, 1H), 7.46 (t, J = 8 Hz, 1H), 7.40 (d, J = 8 Hz, 2H), 7.14-7.10 (m, 5H), 7.08-7.05 (m, 2H), 7.00-6.94 (m, 4H), 6.89 (s, 1H), 6.84 (d, J = 16 Hz, 1H), 6.68-6.63 (m, 4H), 3.75 (d, J = 2 Hz, 6H). ^{13}C NMR (101 MHz, $CDCl_3$) δ (ppm): 158.17, 158.10, 157.48, 152.82, 152.31, 144.12, 142.77, 140.65, 138.51, 137.03, 136.20, 134.67, 133.30, 132.60, 132.01, 131.44, 128.43, 127.78, 127.37, 126.23, 126.11, 125.97, 125.81, 118.60, 118.30, 117.82, 116.82, 115.74, 113.10, 112.98, 106.90, 55.10. HRMS (MALDI-TOF): *m/z* calcd. for $C_{48}H_{34}N_2O_3$: 686.2569; found: 686.2565.

Synthesis of Afterglow Luminescent Nanodots. To prepare AGL AIE dots, TPE-Ph-DCM (0.48 mg, 0.7 μmol), compound **3** (0.50 mg, 1.4 μmol) and DSPE-PEG_{2000} (6.0 mg) were completely dissolved in 1 mL of tetrahydrofuran (THF), which was added into 9 mL of Milli-Q water slowly under continuous sonication by using a microtip probe sonicator (60 W output, XL2000, Misonix Incorporated, NY). The mixture was further sonicated for another 1 minute, and then the THF was removed by evaporation under nitrogen atmosphere at room temperature. The AGL AIE dot suspension was conducted for ultrafiltration (molecular weight cutoff 100 kDa), followed by filtration by a 0.45 μm syringe driven filter. Afterward, the AGL AIE dot suspension was concentrated to 1 mL as a stock solution and stored at 4 ^{o}C in dark. Before the in vitro and in vivo afterglow imaging experiments, the AGL AIE dots were pre-irradiated by white light (400-700 nm) with a power density of 0.2 W cm^{-2} for 2 min. In addition, **3** dots, TPE-Ph-DCM dots, and AGL ACQ dots with [compound **3**]/[Ph-DCM] = 2:1 were prepared following the same procedure as that for the preparation of AGL AIE dots.

Computational Details. All density functional theory (DFT) calculations were performed using Gaussian 09.[5] The geometries and frequency calculations were performed using the B3LYP[6] density functional in conjunction with the 6-31G(d) basis set. Frequency calculations confirmed that optimized structures are minima (no imaginary frequency). To obtain more accurate electronic energies, single-point energy calculations were performed at the B3LYP/6-311+G (2d, p) level of theory with the optimized structures. HOMO and LUMO were visualized by VMD.[7]

In Vitro Fluorescence and Afterglow Luminescence Imaging. In vitro afterglow imaging and fluorescence imaging were performed using the Xenogen IVIS® Lumina II system under bioluminescence and fluorescence modes, respectively. For in vitro fluorescence

imaging of the samples, the fluorescence images were acquired with the filter of Cy 5.5 upon excitation at 465 nm. For in vitro afterglow imaging of the nanodots, the afterglow images were acquired for 20 s with an open filter.

Cell Culture. The murine 4T1 breast cancer cells were purchased from American Type Culture Collection (ATCC). The cancer cells were cultured in RPMI-1640 medium supplemented with 10% fetal bovine serum (FBS), 10 U/mL penicillin and 10 mg/mL streptomycin. The cells were regularly checked for mycoplasma contamination and maintained in an atmosphere of 5% CO_2 and 95% humidified air at 37 ^oC.

Cytotoxicity Study. The 3-(4,5-dimethylthiazol-2-yl)-2,5-diphenyl tetrazolium bromide (MTT) assay was employed to evaluate the cytotoxicity of AGL AIE dots against 4T1 cancer cells. In brief, 4T1 cancer cells were seeded in 96-well plates (Costar, IL, USA) at a density of 4×10^4 cells/mL, respectively. After 24 h incubation, both cells were exposed to a series of doses of AGL AIE dots. At 48 h post addition of AGL AIE dots, the wells were washed with 1 × PBS buffer and 100 μL of freshly prepared MTT solution (0.5 mg/mL) in culture medium was added into each well. The MTT medium solution was carefully removed after 3 h incubation in the incubator. DMSO (100 μL) was then added into each well and the plate was gently shaken for 10 min at room temperature to dissolve all the precipitates formed. The absorbance of MTT at 570 nm was then monitored by the microplate Reader (GENios Tecan). Cell viability was expressed by the ratio of the absorbance of cells incubated with samples to that of the cells incubated with culture medium only.

Animals and Tumor-Bearing Mouse Model. All animal studies were performed in compliance with the guidelines set by Tianjin Committee of Use and Care of Laboratory Animals and the overall project protocols were approved by the Animal Ethics Committee of

Nankai University. Six-week-old female BALB/c mice were purchased from Laboratory Animal Center of the Academy of Military Medical Sciences (Beijing, China). To establish peritoneal carcinomatosis-bearing mouse model, 3×10^5 4T1 cancer cells in 0.1 mL of PBS buffer were intraperitoneally injected into the BALB/c mice. Tumors were grown for approximately 5 days followed by imaging or surgical treatment experiments.

In Vivo Toxicity Assessment. Healthy BALB/c mice were used to evaluate the in vivo toxicity of the NIR-emitting AGL AIE dots, which were randomly assigned into 2 groups (n = 4 per group; two groups were named as AGL AIE dots and untreated groups). Then, 150 μL of the AGL AIE dots (2.8 mM based on compound **3**, two times higher concentration than that used for afterglow imaging) were injected into each healthy mouse in two groups via the tail vein. The mouse weights in two groups were monitored within 7 days. On day 7 post-injection, all the mice in two groups were sacrificed and the blood was collected through cardiac puncture at time of sacrifice for blood chemistry analyses by Tianjin First Central Hospital. Furthermore, on day 7, the normal tissues including liver, spleen and kidneys of each mouse were excised, which were subsequently fixed in 10% neutral buffered formalin, processed routinely into paraffin, sliced at thickness of 4 μm, and stained with hematoxylin and eosin (H&E). The H&E-stained slices were imaged by optical microscopy and assessed by 3 independent pathologists in the hospital.

In Vivo Fluorescence and Afterglow Imaging of Tumors. The peritoneal carcinomatosis-bearing mice were intravenously injected with 150 μL of AGL AIE dots (1.4 mM based on compound **3**). At 2 h post-injection, the mice were sacrificed and major tissues were resected for both afterglow and fluorescence imaging at the same time (n = 3 mice). Alternatively, at 2 h post-injection, the peritoneal carcinomatosis-bearing mice were

anesthetized. Subsequently, the abdomen cavity of mice was opened, followed by fluorescence and afterglow imaging. In vivo afterglow imaging and fluorescence imaging were performed using the Xenogen IVIS® Lumina II system under bioluminescence and fluorescence modes, respectively. In vivo acquisition of fluorescence images was carried out with the filter of Cy 5.5 upon excitation at 465 nm. Moreover, the in vivo afterglow images were acquired for 180 s with an open filter. The fluorescence and afterglow signals were quantified in units of maximum photons per second per square centimeter per steridian.

Afterglow Image-Guided Cancer Surgery. After 150 μL of AGL AIE dots (1.4 mM based on compound **3**) were injected into the peritoneal carcinomatosis-bearing mice via the tail vein for 2 h, the tumor resection surgery was firstly performed according to the experience of a surgeon from Tianjin First Central Hospital (Tianjin, China) without imaging guidance (unguided surgery). This was followed by a second surgery to the same mice guided by the afterglow luminescence emitted from AGL AIE dots. The excised tumor nodules were analyzed by afterglow luminescence imaging. The tumor sizes resected from the first and second surgery were also quantified. The survival of the mice in both unguided surgery (9 mice) and afterglow image-guided surgery (12 mice) groups was then monitored.

Histological Study. The excised tissues by the surgeon from mice in afterglow image-guided surgery group were performed for histological analysis. Briefly, the tissues were fixed in 10% neutral buffered formalin, processed routinely into paraffin, sectioned at a thickness of 5 μm, and stained with hematoxylin and eosin (H&E). The slices were examined by a digital microscope (Leica QWin) and assessed by 3 independent pathologists, in order to determine whether the excised tissues are tumors.

Statistical Analysis. Quantitative data were expressed as mean ± standard deviation (s.d.). Statistical comparisons were made by ANOVA analysis and two-sample Student's *t*-test. *P* value < 0.05 was considered statistically significant.

Reference

(1) Green, O.; Eilon, T.; Hananya, N.; Gutkin, S.; Bauer, C. R.; and Shabat, D. *ACS Cent. Sci.* **2017**, *3*, 349.

(2) Zheng, Y.; Zhao, M.; Qiao, Q.; Liu, H.; Lang, H. and Xu, Z. *Dyes and Pigments* **2013,** *98*, 367.

(3) Zhang, C.-J.; Hu, Q.; Feng, G.; Zhang, R.; Yuan, Y.; Lua, X. and Liu, B. *Chem. Sci.* **2015**, *6*, 4580.

(4) Jana, D.; Boxi, S.; Paruib, P. P. and Ghorai, B. K. *Org. Biomol. Chem.* **2015**, *13*, 10663.

(5) Frisch, M. J.; Trucks, G. W.; Schlegel, H. B.; Scuseria, G. E.; Robb, M. A.; Cheeseman, J. R.; Scalmani, G.; Barone, V.; Mennucci, B.; Petersson, G. A.; Nakatsuji, H.; Caricato, M.; Li, X.; Hratchian, H. P.; Izmaylov, A. F.; Bloino, J.; Zheng, G.; Sonnenberg, J. L.; Hada, M.; Ehara, M.; Toyota, K.; Fukuda, R.; Hasegawa, J.; Ishida, M.; Nakajima, T.; Honda, Y.; Kitao, O.; Nakai, H.; Vreven, T.; Montgomery, J. A., Jr.; Peralta, J. E.; Ogliaro, F.; Bearpark, M.; Heyd, J. J.; Brothers, E.; Kudin, K. N.; Staroverov, V. N.; Kobayashi, R.; Normand, J.; Raghavachari, K.; Rendell, A.; Burant, J. C.; Iyengar, S. S.; Tomasi, J.; Cossi, M.; Rega, N.; Millam, J. M.; Klene, M.; Knox, J. E.; Cross, J. B.; Bakken, V.; Adamo, C.; Jaramillo, J.; Gomperts, R.; Stratmann, R. E.; Yazyev, O.; Austin, A. J.; Cammi, R.; Pomelli, C.; Ochterski, J. W.; Martin, R. L.; Morokuma, K.; Zakrzewski, V. G.; Voth, G. A.; Salvador, P.; Dannenberg,

J. J.; Dapprich, S.; Daniels, A. D.; Farkas, O.; Foresman, J. B.; Ortiz, J. V.; Cioslowski, J.; Fox, D. J. *Gaussian 09, revision D.01*; Gaussian, Inc., Wallingford, CT, 2013.

(6) (a) Becke, A. D. *J. Chem. Phys*. **1993**, *98*, 5648. (b) Becke, A. D. *J. Chem. Phys.* **1993**, *98*, 1372. (c) Becke, A. D. *J. Chem. Phys*. **1988**, *38*, 3098. (d) Lee, C.; Yang, W.; Parr, R. G. *Phys. Rev. B* **1988**, *37*, 785.

(7) Humphrey, W.; Dalke, A.; Schulten, K. *J. Mol. Graphics* **1996**, *14*, 33.

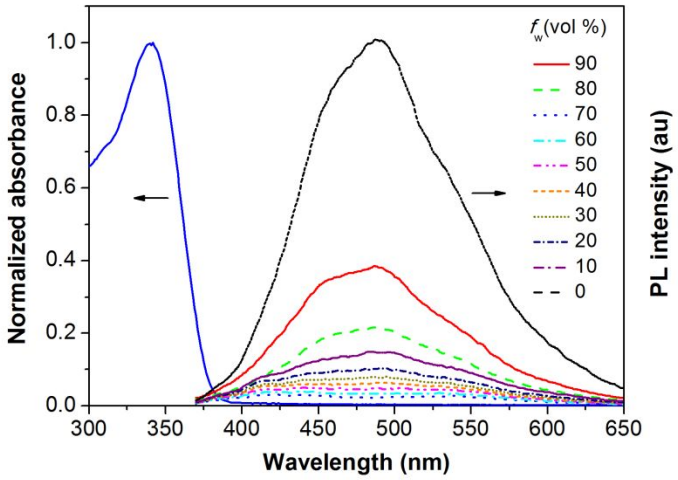

Figure S1. UV-vis absorption and photoluminescence (PL) spectra of compound **3** (10 μM) in pure THF and its PL spectra in THF/water mixtures with different water fractions.

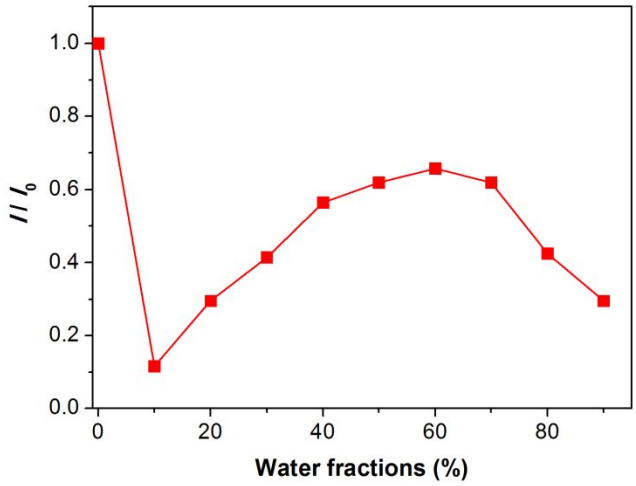

Figure S2. Plot of I/I_0 versus water fraction. I_0 and I are the maximum PL intensities of compound **4** (10 μM) in pure THF and THF/water mixtures, respectively.

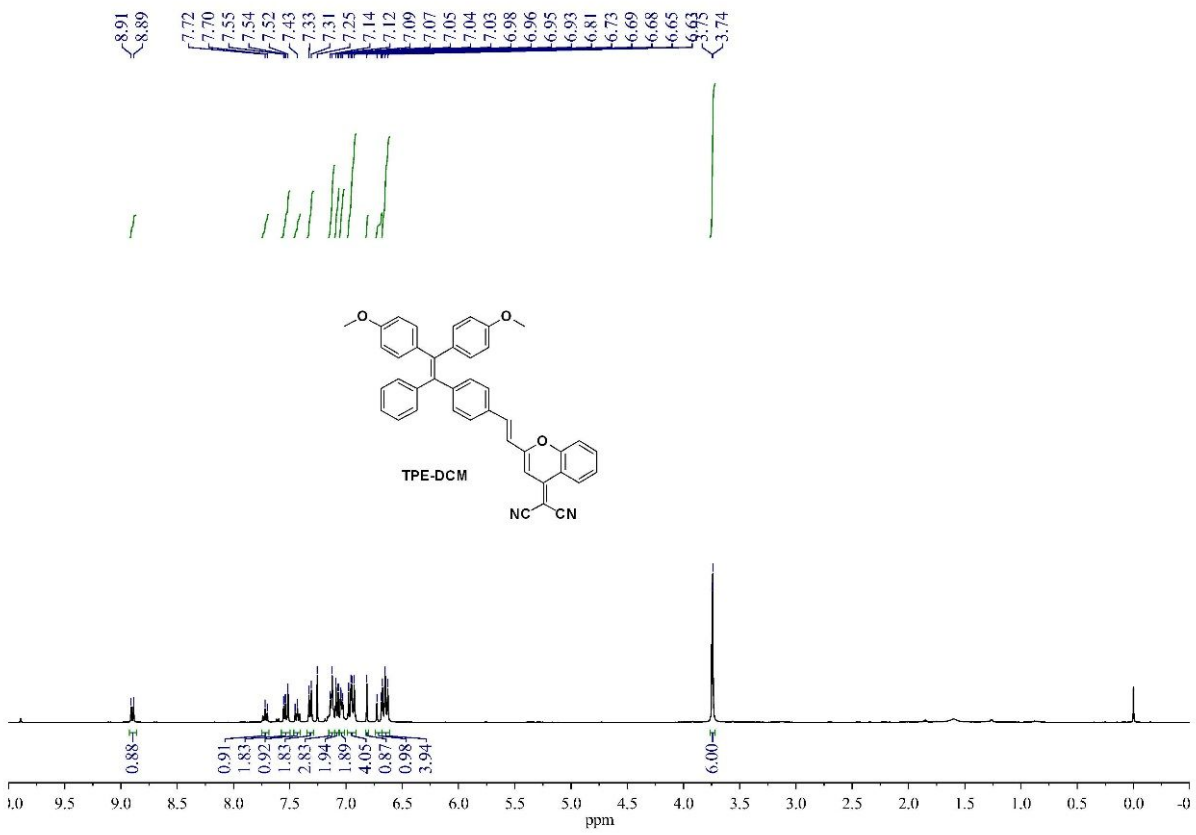

Figure S3. ^{1}H NMR spectrum of TPE-DCM.

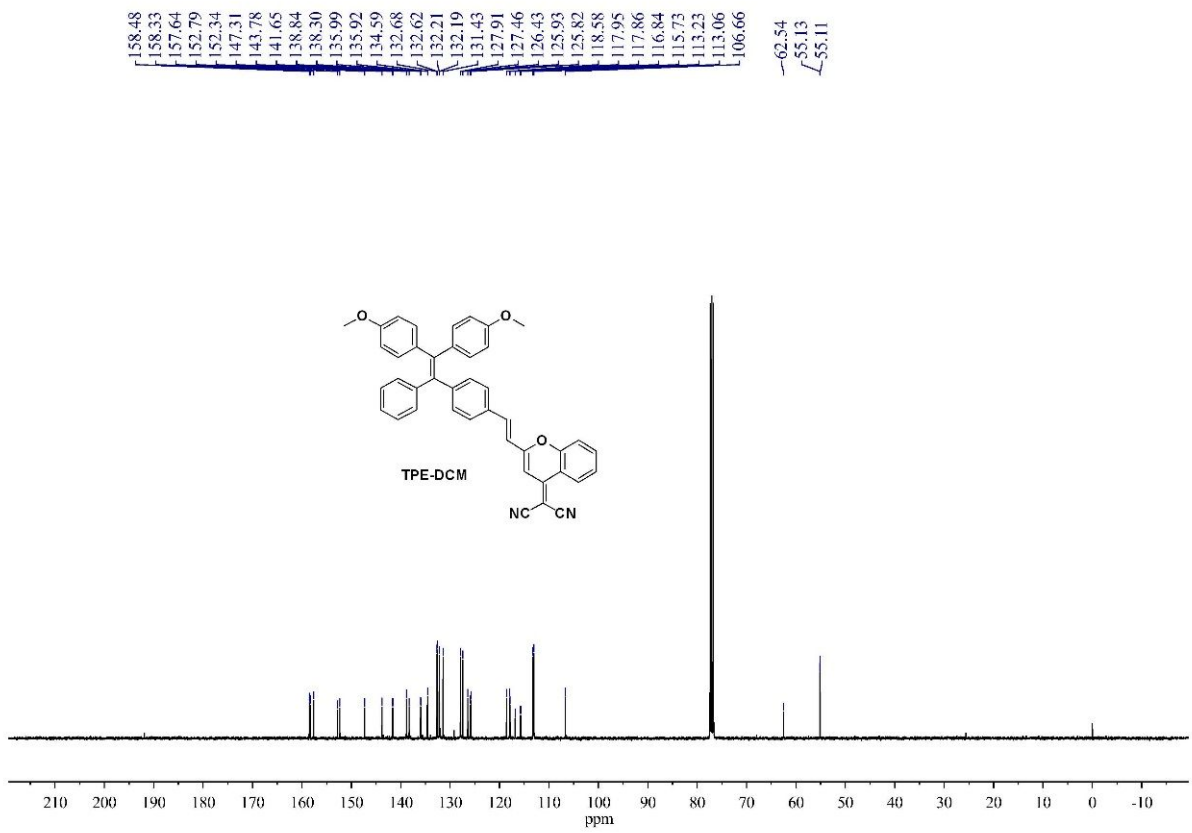

Figure S4. ^{13}C NMR spectrum of TPE-DCM.

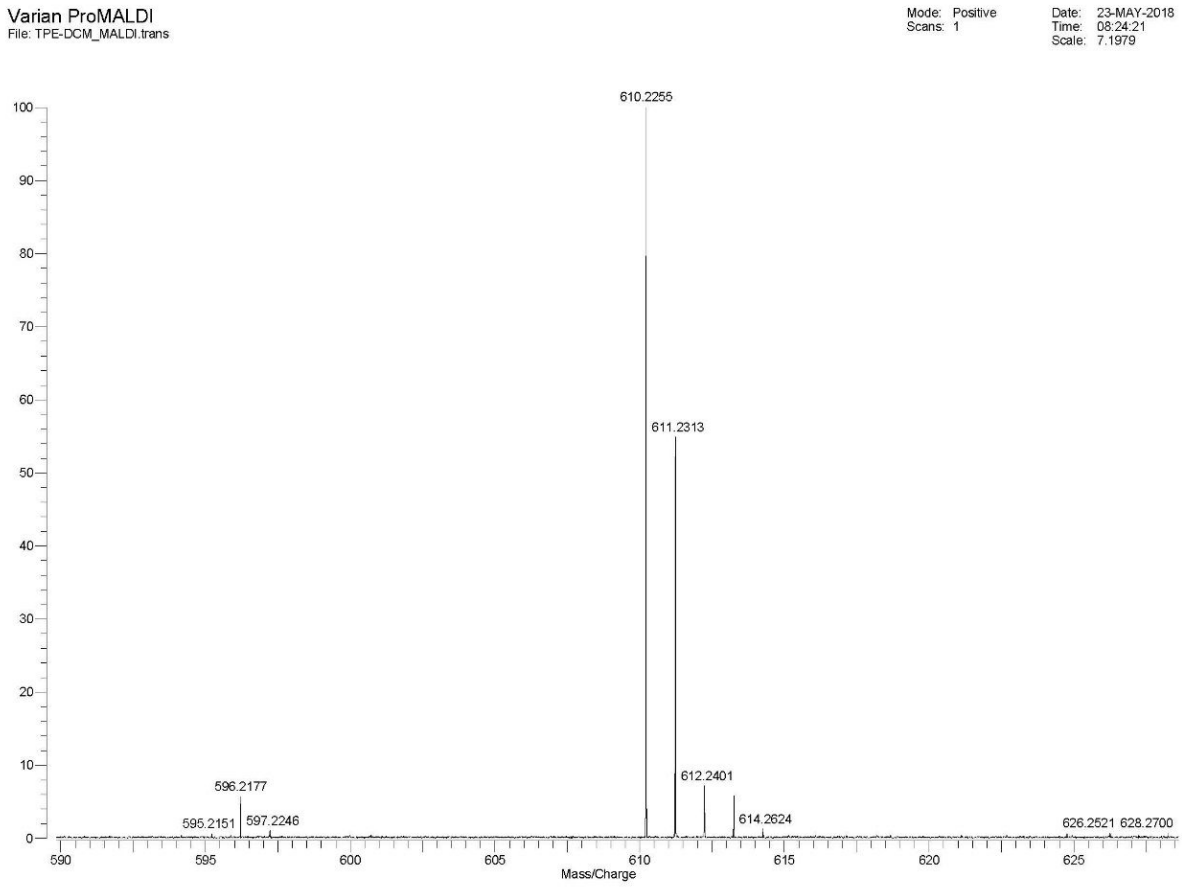

Figure S5. HRMS (MALDI-TOF) spectrum of TPE-DCM.

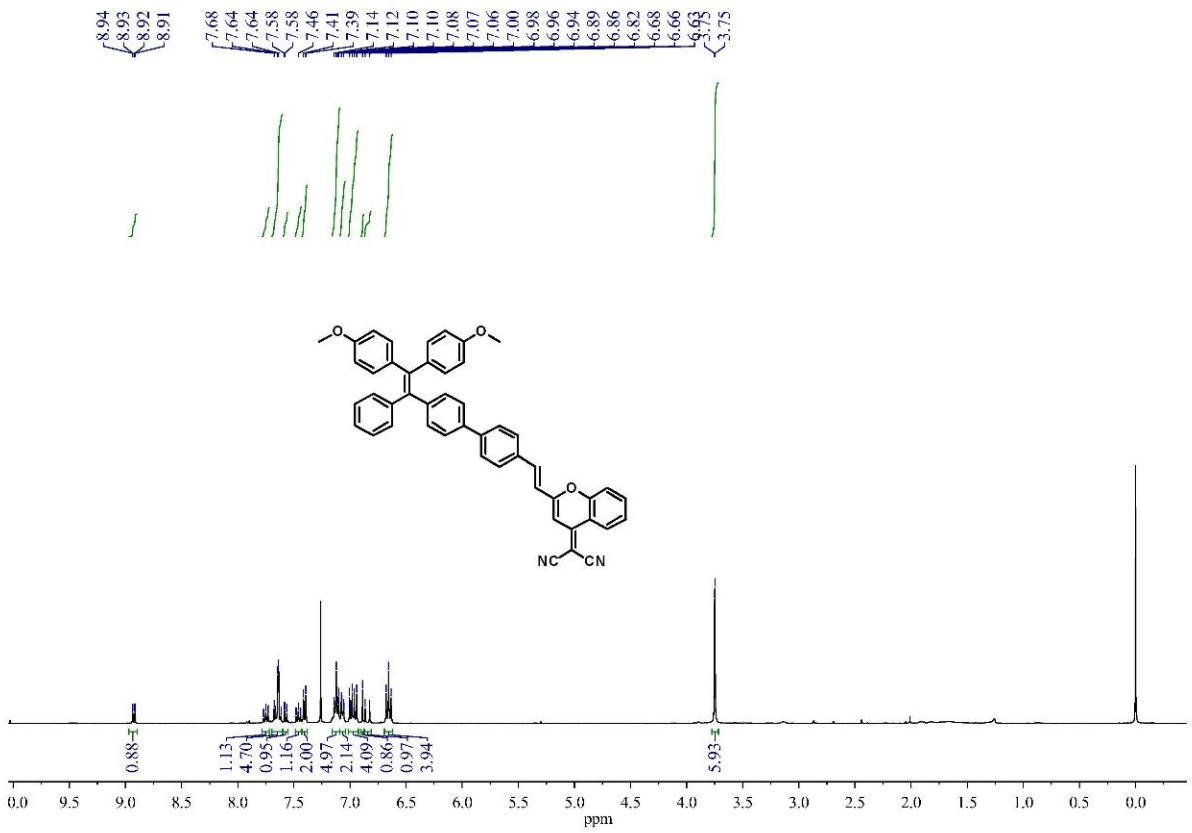

Figure S6. ^{1}H NMR spectrum of TPE-Ph-DCM.

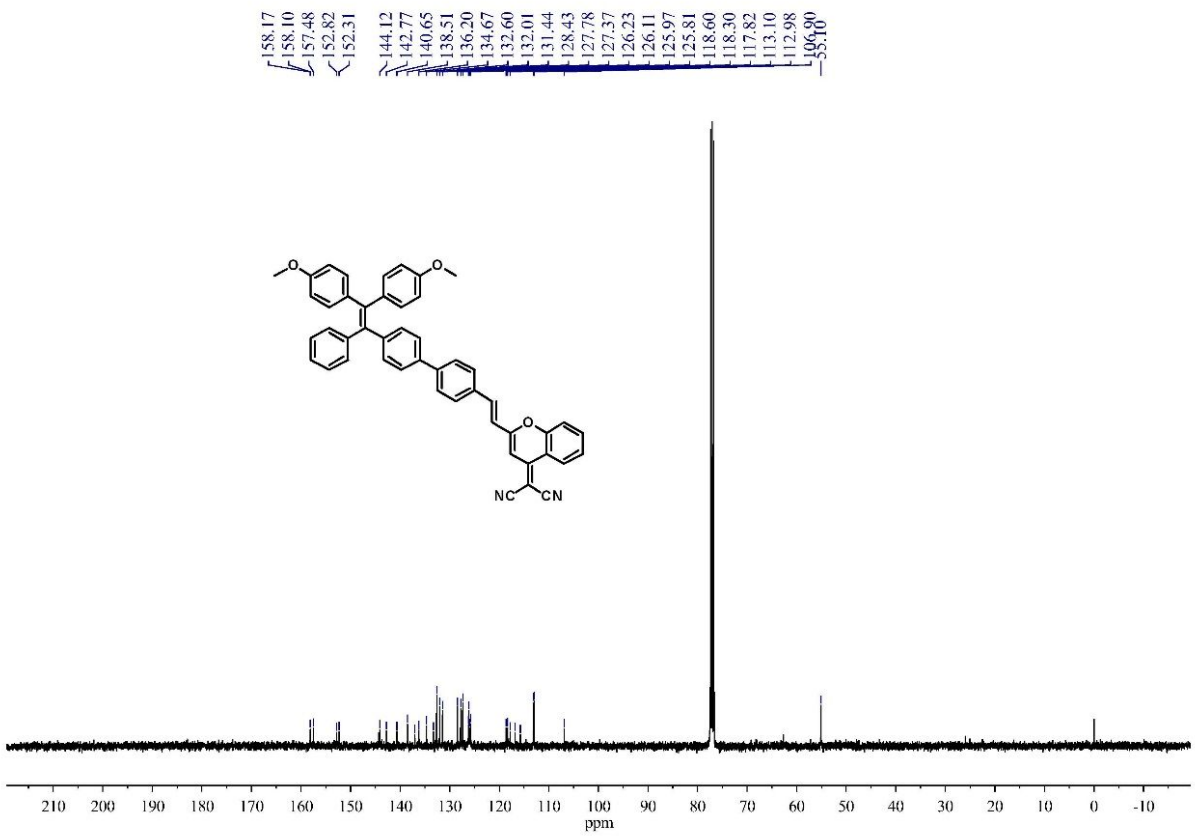

Figure S7. ^{13}C NMR spectrum of TPE-Ph-DCM.

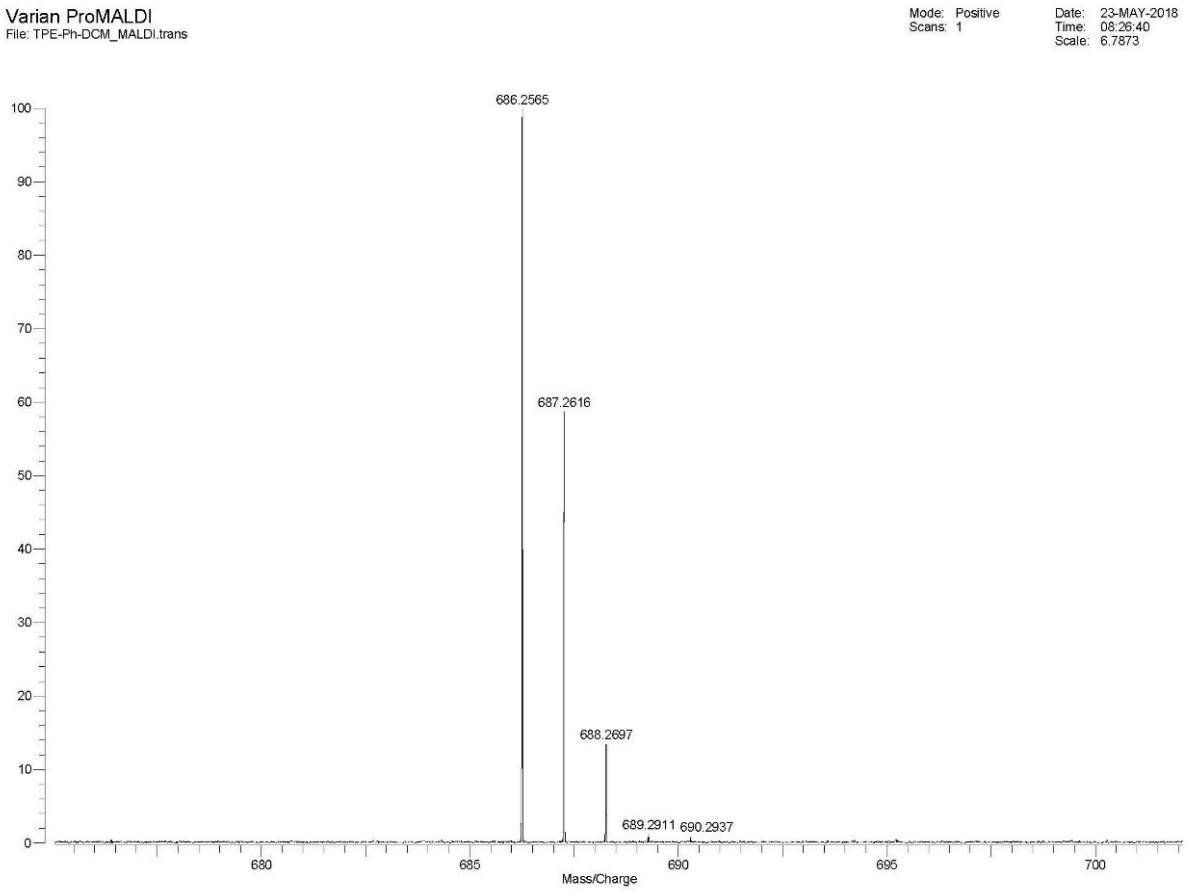

Figure S8. HRMS (MALDI-TOF) spectrum of TPE-Ph-DCM.

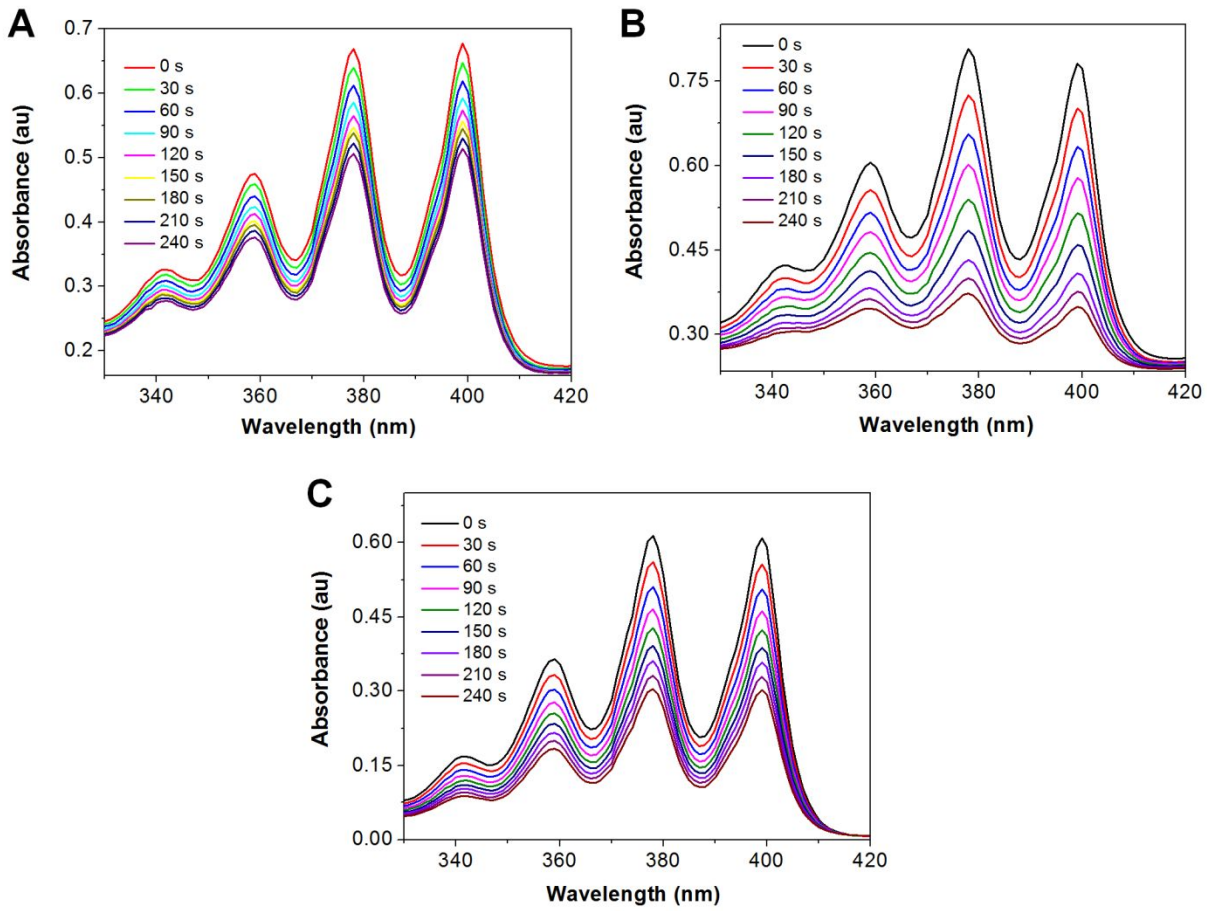

Figure S9. UV-vis absorption spectra of ABDA (50 μM) in the presence of (A) TPE-DCM (10 μM), (B) TPE-Ph-DCM (10 μM) or (C) Rose Bengal (10 μM) under white light irradiation (0.2 W/cm^2) for 0-240 s.

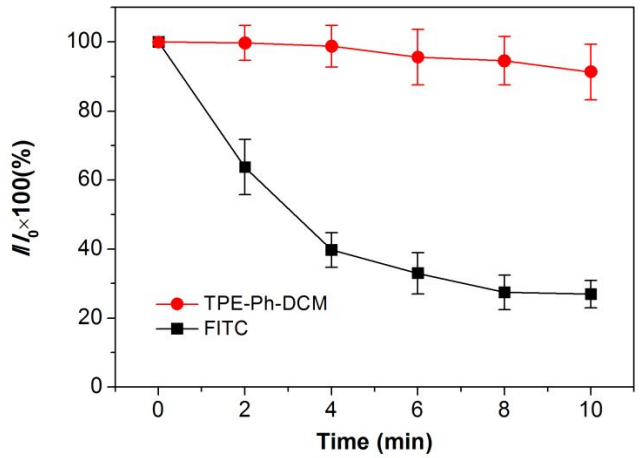

Figure S10. Photostability of TPE-Ph-DCM-loaded lipid-PEG_{2000} nanoparticles in 4T1 cancer cells upon continuous exposure to 488 nm (1.25 mW) laser for 10 min. Fluorescein isothiocyanate (FITC) was used as a control and its photostability was studied by the same experimental condition as that for TPE-Ph-DCM. I_0 is the initial PL intensity; and I is the PL intensity at different exposure time.

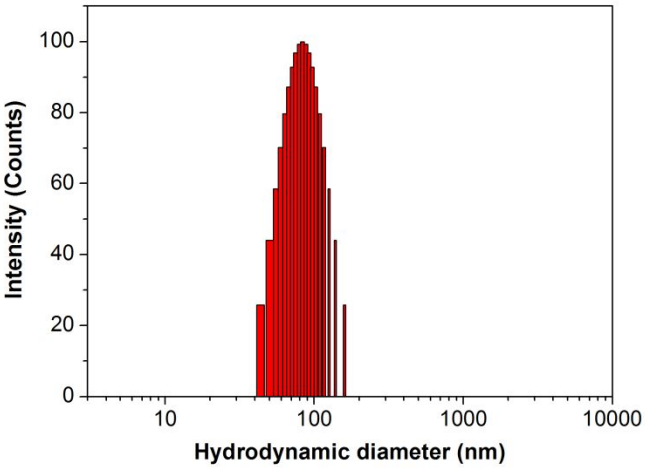

Figure S11. Hydrodynamic diameter distribution measured by DLS of the compound **3**/TPE-Ph-DCM co-loaded lipid-PEG_{2000} nanoparticles before exposure to white light.

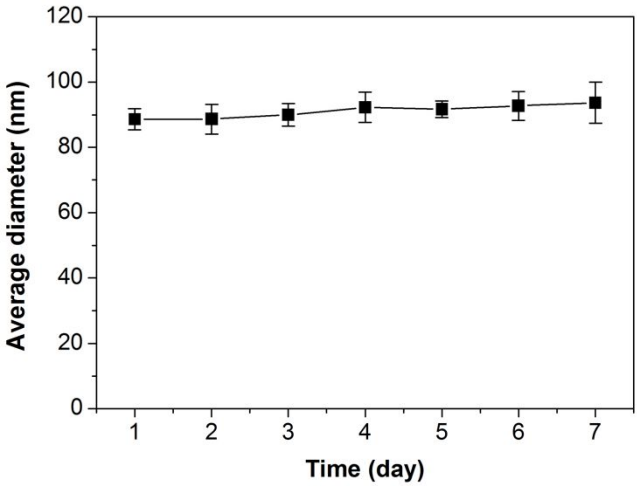

Figure S12. Hydrodynamic diameter change of the AGL AIE dots during one-week study duration measured by DLS.

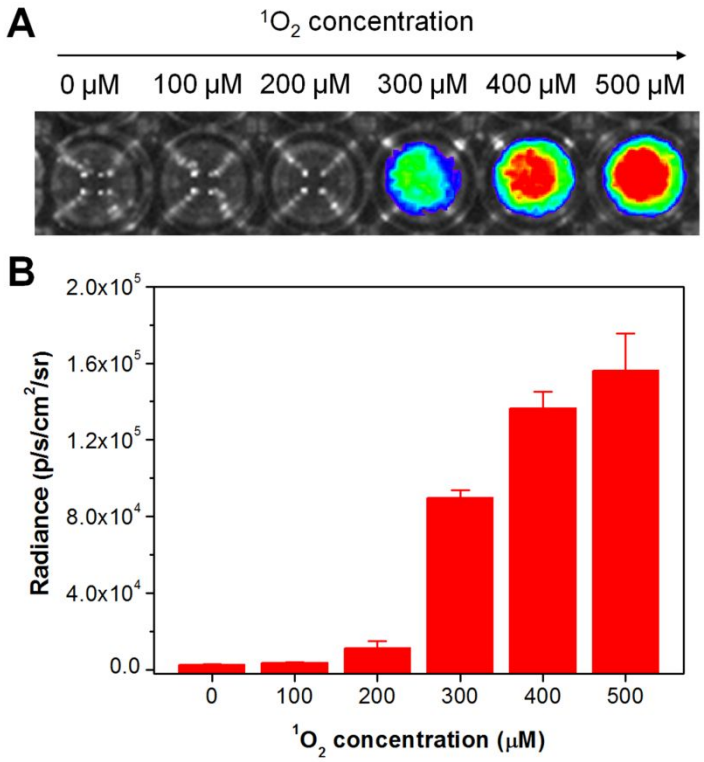

Figure S13. (A) Afterglow imaging and (B) the quantitative data of the compound **3**/TPE-Ph-DCM co-loaded lipid-PEG_{2000} nanoparticles (50 μM based on compound **3** with [compound

3]/[TPE-Ph-DCM] = 2:1) after addition of various concentrations of $^1O_2$ ranging from 0-500 μM. The $^1O_2$ is quantitatively prepared from H_2O_2-NaOCl system according to the literature (*J. Am. Chem. Soc.* **1978**, *100*, 5732-5740; *Chem. Commun.* **2011**, *47*, 7386–7388; *J. Am. Chem. Soc.* **2004**, *126*, 11543-11548).

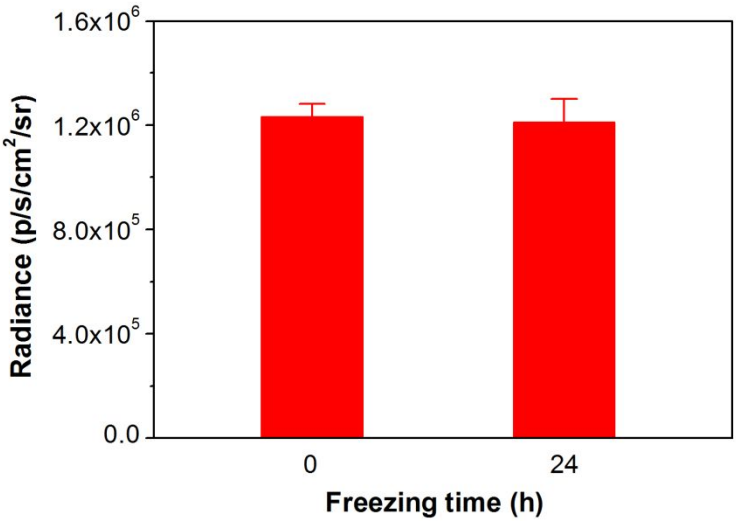

Figure S14. Afterglow intensity of the AGL AIE dots after preservation at -20 °C for 0 and 24 h. After white light (0.2 W/cm^2) pre-irradiation for 2 min, the AGL AIE dots (50 μM based on compound **3** with [compound **3**]/[TPE-Ph-DCM] = 2:1) were stored at -20 °C for 0 (without freezing storage) and 24 h, which was followed by warming to 37 °C and imaged by IVIS system under bioluminescent mode. The result indicates that the afterglow intensity is negligibly reduced after 24 h frozen storage.

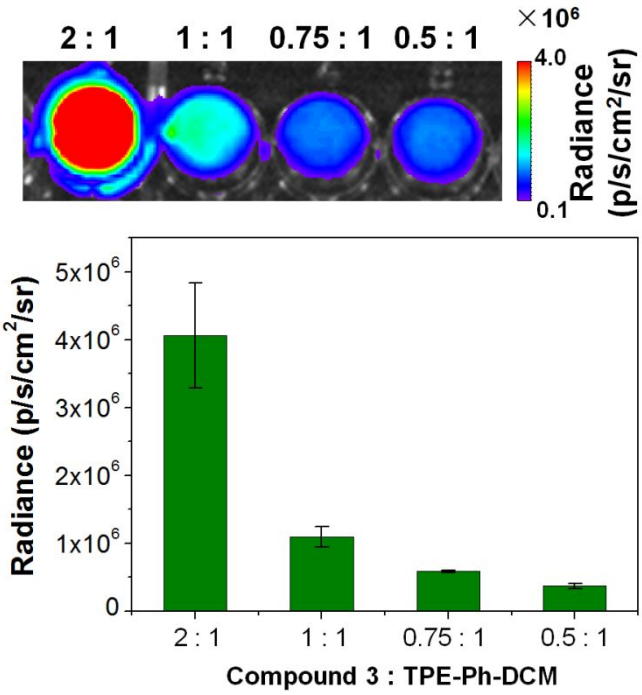

Figure S15. Afterglow images and quantitative data of AGL AIE dots with various encapsulated molar ratio between compound **3** and TPE-Ph-DCM (from 0.5:1 to 2:1) in PBS at 37 °C at 1 min post white light pre-irradiation.

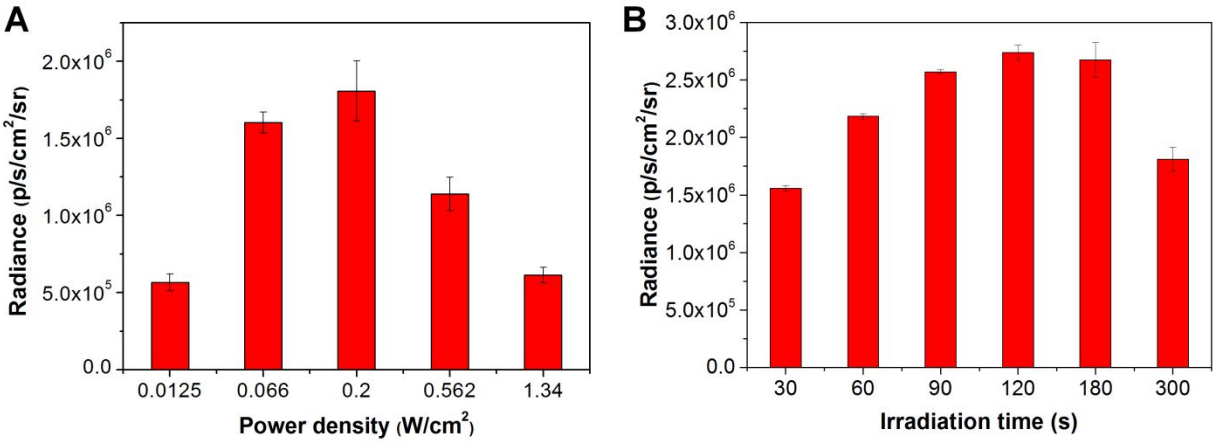

Figure S16. (A) Afterglow luminescence of AGL AIE dots (100 μM based on compound **3** with [compound **3**]/[TPE-Ph-DCM] = 2:1) after white light irradiation at different power densities for 60 s. (B) Afterglow luminescence of AGL AIE dots (100 μM based on compound

3 with [compound **3**]/[TPE-Ph-DCM] = 2:1) at different light irradiation time at a light power density of 0.2W/cm^2. Error bars, mean ± s.d. (n = 3).

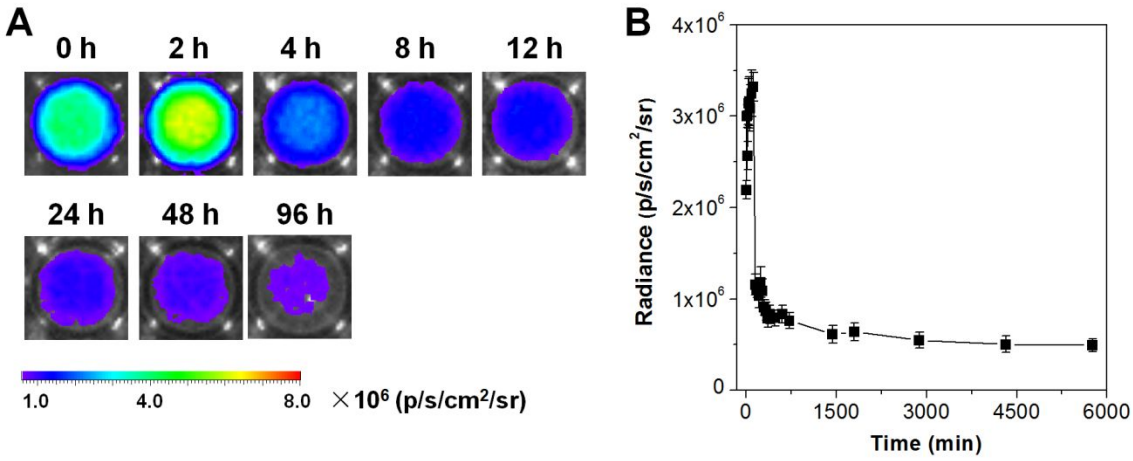

Figure S17. (A) Afterglow decay images of **10** dots in PBS at 37 °C. (B) Plot of afterglow intensity versus time according to the quantitative results in (A).

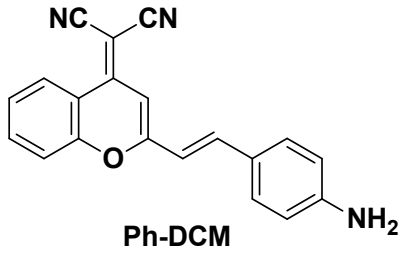

Figure S18. Chemical structure of Ph-DCM.

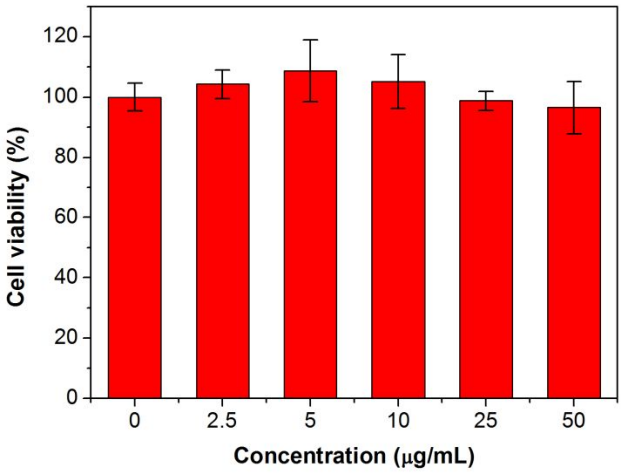

Figure S19. Cell viabilities of 4T1 cancer cells after incubation with different concentrations of AGL AIE dots for 48 h. The concentration is based on compound **3** in the dots with 50 μg/mL representing 0.14 mM. Error bars, mean ± s.d. (n = 3).

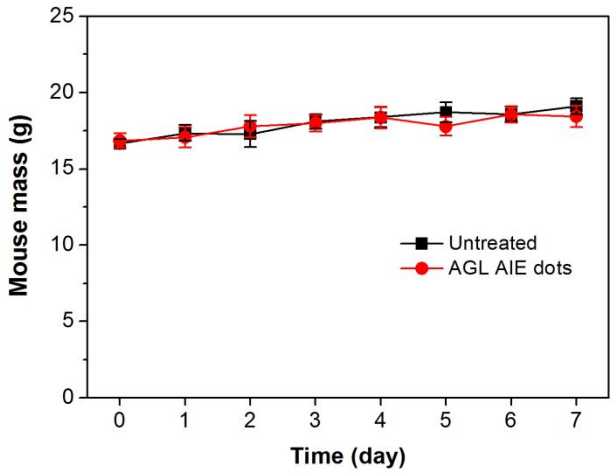

Figure S20. Body weight changes of the healthy mice with and without intravenous injection of AGL AIE dots (n = 4 mice in each group). The result reveals that no body weight loss was observed for AGL AIE dot-treated mice.

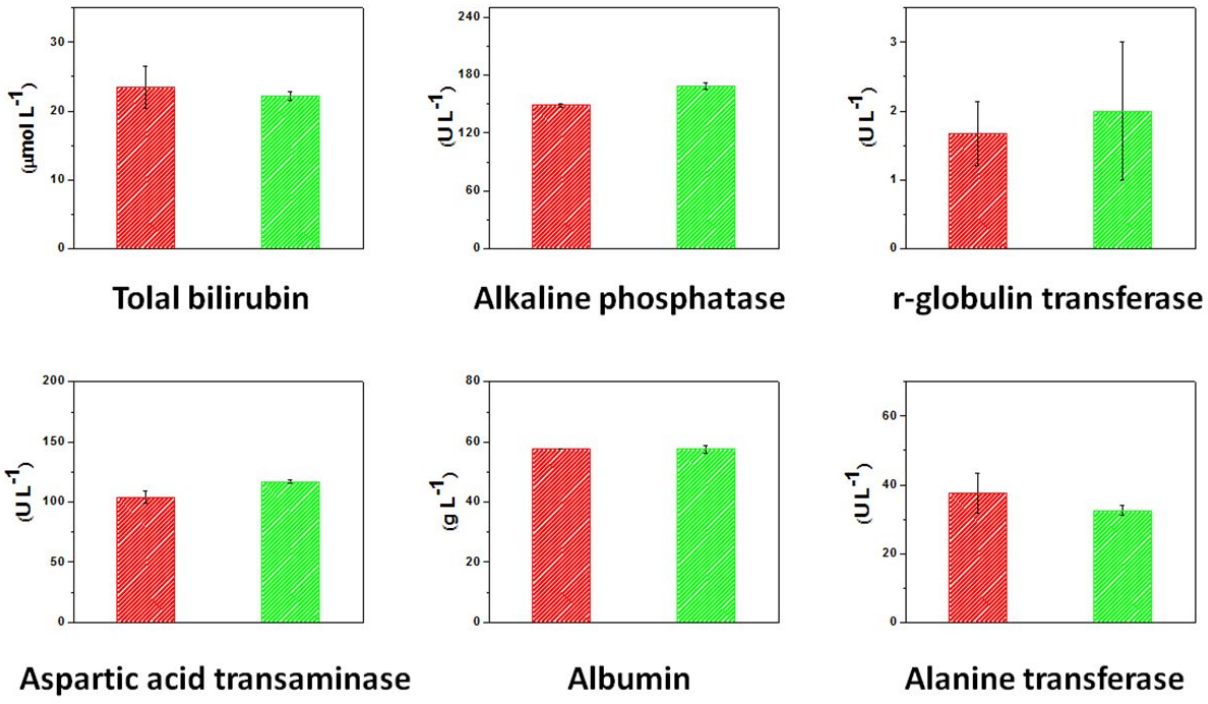

Figure S21. Blood test parameters regarding to the liver function of the healthy mice with and without intravenous injection of AGL AIE dots (n = 4 mice in each group). The result reveals that there is no difference in each parameter between the groups of untreated (green) and AGL AIE dot-treated mice (red).

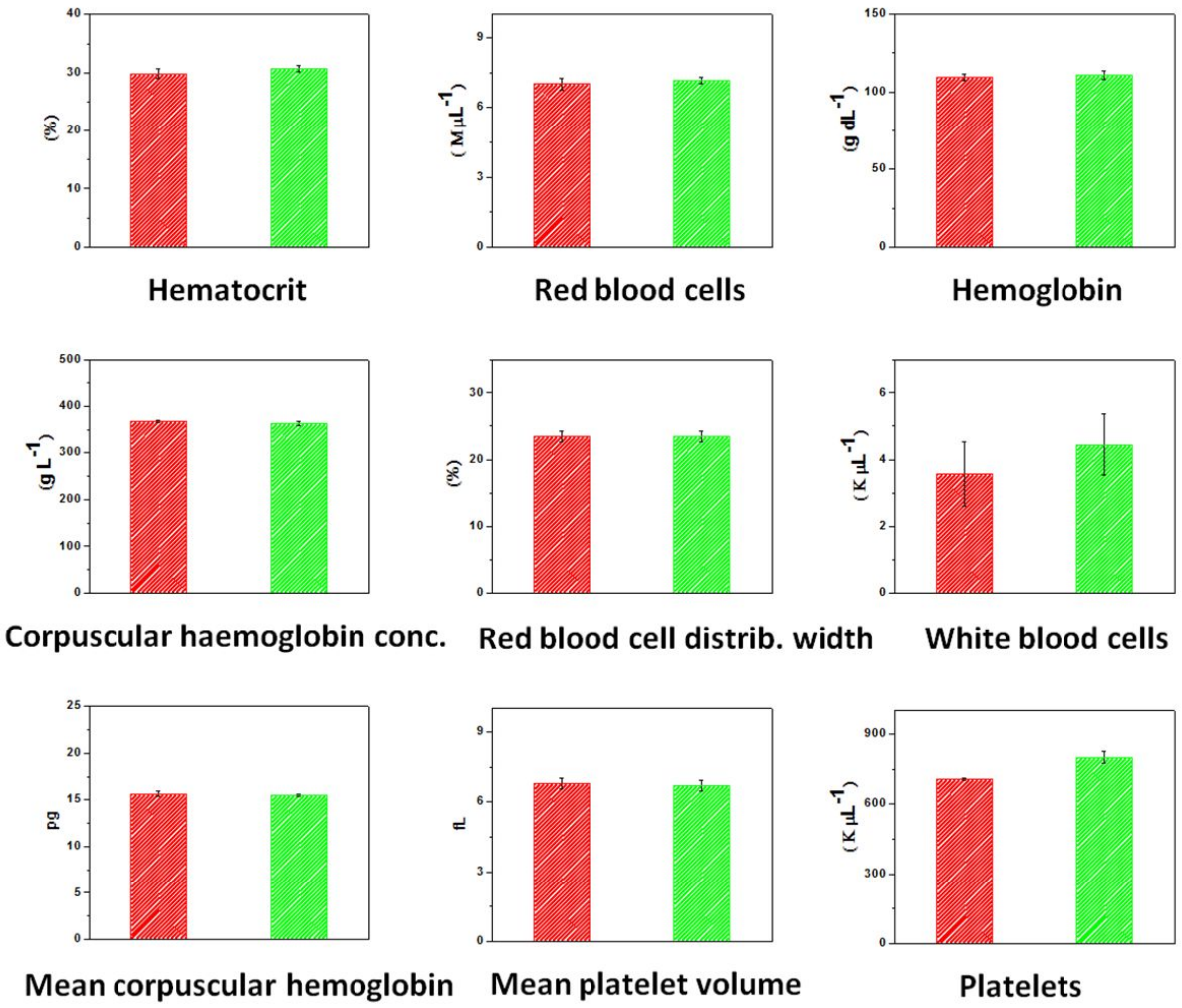

Figure S22. Blood test parameters regarding to the red blood cell, haem regulation and white blood cell count of the healthy mice with and without intravenous injection of AGL AIE dots (n = 4 mice in each group). conc.: concentration; distrib.: distribution. The result reveals that there is no difference in each parameter between the groups of untreated (green) and AGL AIE dot-treated mice (red).

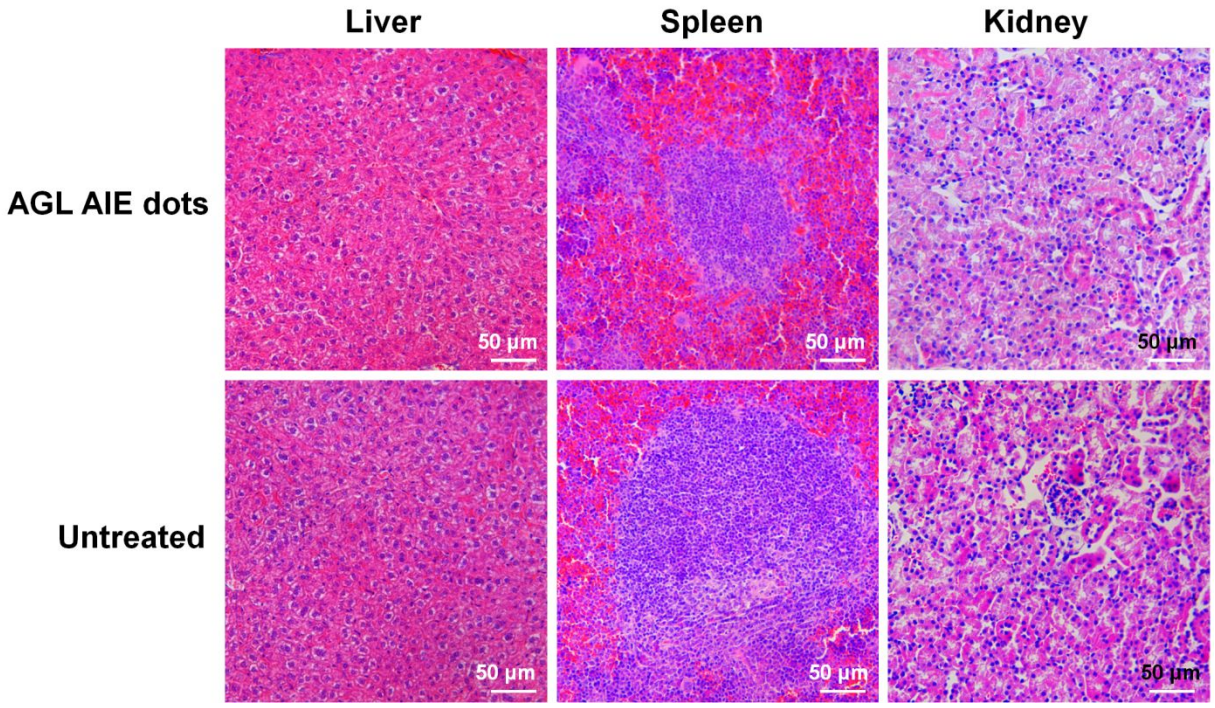

Figure S23. Representative images of H&E-stained normal organ slices from untreated and AGL AIE dot-treated mice. The result indicates that intravenous administration of AGL AIE dots does not lead to obvious lesions to liver, spleen and kidney tissues.

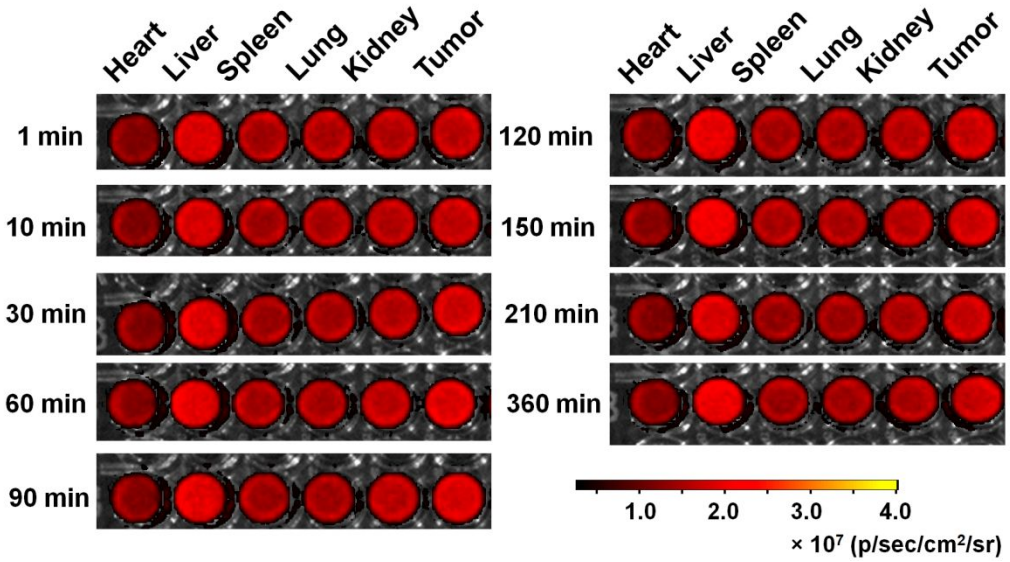

Figure S24. The NIR fluorescent images (with the filter of Cy 5.5 upon excitation at 465 nm) of AGL AIE dots in different tissue homogenates (tissue concentration of 30 mg/mL) over time.